Probing the precise location of the radio core in the TeV blazar Mrk 501 with VERA at 43 GHz

Shoko Koyama,[1,2,3,4,*] Motoki Kino,[5,3] Akihiro Doi,[3] Kotaro Niinuma,[6] Kazuhiro Hada,[2,7] Hiroshi Nagai,[2] Mareki Honma,[2] Kazunori Akiyama,[1,2] Marcello Giroletti,[7] Gabriele Giovannini,[7,8] Monica Orienti,[7] Naoki Isobe,[3] Jun Kataoka,[9] David Paneque,[10] Hideyuki Kobayashi,[2] and Keiichi Asada[11]

[1]Department of Astronomy, Graduate School of Science, The University of Tokyo, 7-3-1 Hongo, Bunkyo-ku, Tokyo 113-0033, Japan

[2]National Astronomical Observatory of Japan, 2-21-1 Osawa, Mitaka, Tokyo 181-8588, Japan

[3]Institute of Space and Astronautical Science, Japan Aerospace Exploration Agency, 3-1-1 Yoshinodai, Chuou-ku, Sagamihara, Kanagawa 252-5210, Japan

[4]Max-Planck-Institut für Radioastronomie, Auf dem Hügel 69, D-53121 Bonn, Germany

[5]Korea Astronomy and Space Science Institute, 776 Daedeokdae-ro, Yuseong-gu, Daejeon, 305-348, Republic of Korea

[6]Graduate School of Science and Engineering, Yamaguchi University, Yamaguchi 753-8511, Japan

[7]INAF Istituto di Radioastronomia, via Gobetti 101, 40129 Bologna, Italy

[8]Dipartimento di Astronomia, Università di Bologna, via Ranzani 1, I-40127 Bologna, Italy

[9]Research Institute for Science and Engineering, Waseda University, 3-4-1 Okubo, Shinjuku, Tokyo 169-8555, Japan

[10]Max-Planck-Institut für Physik, Föhringer Ring 6, D-80805 München, Germany

[11]Institute of Astronomy and Astrophysics, Academia Sinica Institute of Astronomy and Astrophysics, P.O. Box 23-141, Taipei 10617, Taiwan

*E-mail: skoyama@mpifr-bonn.mpg.de

Abstract

We investigate the position of the radio core in a blazar by multi-epoch astrometric observations at 43 GHz. Using the VLBI Exploration of Radio Astrometry (VERA), we have conducted four adjacent observations in 2011 February and another four in 2011 October, and succeeded in measuring the position of the radio core in the TeV blazar Mrk 501 relative to a distant compact quasar NRAO 512. During our observations, we find that (1) there is no positional change within $\sim$0.2 mas or $\sim$2.0 pc de-projected with $\pm 1\sigma$ error for the weighted-mean phase-referenced positions of the Mrk 501 core relative to NRAO 512 over four adjacent days, and (2) there is an indication of position change for the 3C 345 core relative to NRAO 512. By applying our results to the standard internal shock model for blazars, we constrain the bulk Lorenz factors of the ejecta.

Key words: astrometry — galaxies: active — galaxies: individual (Mrk 501 3C 345, NRAO 512) — radio continuum: galaxies — techniques: interferometric

1 Introduction

Locating radio-emitting regions in relativistic jets in active galactic nuclei (AGNs) has been one of the most intriguing issues for exploring the ultimate mechanism of jet formation (e.g., Marscher et al. 2008; Abdo et al. 2010). One of the leading scenarios suggests that the radio cores of blazars correspond to stationary standing shocks located at several parsec scales downstream from the central black holes, based on the delay timescales of the radio core brightening after the precedent γ-ray flares (Marscher et al. 2008; Jorstad et al. 2010; Agudo et al. 2011a, 2011b). On the other hand, phase-referencing Very Long Baseline Array (VLBA) observations of the radio galaxy M 87 revealed that the radio core at 43 GHz is located only $\sim$0.01 pc away from the upstream end of the conical jet (Hada et al. 2011). Nowadays, it is important to explore the origin of such a discrepancy of radio core locations and their stationarity between radio galaxies and blazars.

To explore the locations and their stationarity of radio cores in blazars directly, multi-epoch Very Long Baseline Interferometry (VLBI) astrometric observations are the most powerful and reliable method. By means of astrometric observations, we can measure the positions of target sources relative to phase-calibrators close to the targets on the sky. Over the past few decades, astrometric monitoring experiments based on the International VLBI Service for Geodesy and Astrometry (IVS) also have been performed towards the radio cores of more than a hundred blazars (e.g., Ma et al. 1998; Fey et al. 2004; Titov et al. 2011). However, most of these astrometric experiments have been limited at 2.3 and 8 GHz.[1] Hence, little is known about the relative location of the brightness peak and the stationarity seen at higher frequencies.

We should carefully select an appropriate blazar and an observing frequency. It is well known that radio cores of blazars usually tend to be optically thick against synchrotron self-absorption (SSA) at lower frequencies (e.g., Kellermann & Pauliny-Toth 1981; Marscher & Gear 1985). To avoid the SSA effect as much as we can, we select a TeV blazar, Mrk 501 ($z = 0.034$). Mrk 501 is one of the best blazars for this study because the radio core spectrum between 1.4 and 86 GHz measured by VLBI clearly shows convex shape peaking at $\sim$ 8 GHz (figure 8 in Giroletti et al. 2008). Therefore, we can probe the locations of radio-emitting regions and reduce the SSA effect by selecting an observing frequency higher than the peak frequency. We select an observing frequency of 43 GHz, which is the highest frequency for VLBI astrometry, to minimize the SSA effect. The proximity and brightness of

Mrk 501 enable us to perform the precise astrometric observations. Another advantage of this source is that there are two bright phase-calibrators within an angular separation of a few degrees, such that it is made easier to perform phase-referencing observations.

The plan of this paper is as follows. In section 2, we describe our astrometric procedure for measuring the core position of Mrk 501. We explain the observation in section 3, and data reduction in section 4. The results and the discussions are described in sections 5 and 6, respectively. The conclusion and future prospects are given in section 7. The error estimation of the phase-referenced positions is written in the Appendix. Throughout this paper, we adopt the following cosmological parameters; $H_0 = 71 \ \mathrm{km \ s^{-1} Mpc^{-1}}$, $\Omega_M = 0.27$, and $\Omega_\Lambda = 0.73$ (Komatsu et al. 2009), or 1 mas = 0.662 pc for Mrk 501.

2 Astrometric procedure in measuring Mrk 501's core position

In this section, we describe our method to measure the core position of the target source Mrk 501. We chose the distant point source NRAO 512 ($z = 1.66$, 1 mas = 8.56 pc) as a reference position, since the absence of a jet component minimizes the positional change of its location. The angular separation between Mrk 501 and NRAO 512 is $2°57$. Given the angular separation limit of the dual-beam system for VERA is $2°20$, we inserted a bright calibrator 3C 345 ($z = 0.593$, 1 mas = 6.64 pc), separated by $2°09$ from Mrk 501. The source configuration on the celestial sphere is shown in figure 1. Since the flux density of 3C 345 ($\sim$2 Jy) is much higher than that of Mrk 501 ($\sim$300 mJy) and NRAO 512 ($\sim$500 mJy), we chose 3C 345 as a phase
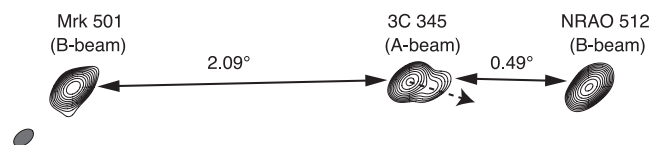

Fig. 1. Source configurations, dual-beam allocations, and self-calibrated images of our VERA astrometric observations at 43 GHz. The three sources quasi-perfectly align within $\sim 3'$ in an east–west direction on the sky. The calibrator 3C 345 was observed in A-beam, and at the same time, Mrk 501 and NRAO 512 were observed in B-beam in every several minutes. Shown are the self-calibrated images of the observed sources stacked over 2011 February 15, 16, 17, and 18. The contours are plotted at 3σ noise level × (−1, 1, 2, 4, . . .). The size of the restored beam (bottom left) is 0.613 mas × 0.366 mas at position angle −53°. The 1σ noise level is 3.04 mJy beam^{-1} for Mrk 501, and 5.15 mJy beam^{-1} for NRAO 512. The 1σ noise level is 30.0 mJy beam^{-1} for 3C 345, which is about 10 times higher than that for Mrk 501 because the image quality of the self-calibrated image is mainly limited by the image dynamic range (the peak flux of 3C 345 is about 10 times higher than that of Mrk 501; see table 2). The dotted arrow shows the innermost jet direction of 3C 345 at a position angle of −103°.

---

[1] See however Lanyi et al. (2010)

Table 1. Summary of VERA 43 GHz astrometric observation.

Epoch	Time range (UT)	Code	Bad weather*
2011/02/15	18:18–02:18	R11046B	OGA: 00:30–01:20, 02:15–02:18, IRK: 00:50–01:40
2011/02/16	18:14–02:14	R11047B	IRK, OGA: 22:00–22:40
2011/02/17	18:10–02:10	R11048B	IRK, ISH : 18:00–23:00
2011/02/18	18:06–02:06	R11049B	IRK, OGA: 23:40–23:58, 00:45–1:07
2011/10/20	01:50–09:50	R11293A	OGA: 01:50–06:00, IRK: 06:00–09:50
2011/10/21	01:46–09:46	R11294A	
2011/10/23	01:38–09:38	R11296A	ISH: 01:38–06:30, 05:30–07:00
2011/10/24	01:34–09:34	R11297A	

*MIZ: Mizusawa, IRK: Iriki, OGA: Ogasawara, ISH: Ishigaki. MIZ couldn't observe Mrk 501 for ∼50 min in every observation due to its elevation limit.

calibrator and applied its fringe phase solutions and structure phase solutions to the other two sources. The two sources, 3C 345 and NRAO 512, are a well-known phase-referencing pair (Shapiro et al. 1979; Bartel et al. 1986; Doi et al. 2006; Jung et al. 2011). Below, we explain our steps to derive the core position of Mrk 501 relative to NRAO 512 for each epoch.

(1) We measured the core position offset from the phase-tracking center on the phase-referenced images of Mrk 501 referenced to 3C 345's core.

(2) We measured the peak position offset from the phase-tracking center on the phase-referenced images of NRAO 512 relative to 3C 345's core.

(3) We subtracted the position offset of (2) from that of (1) to derive the core position of Mrk 501 relative to NRAO 512.

Through this procedure, the position errors arise from 3C 345 were completely cancelled out (for details, see subsection 5.3 and appendix 1.3).

3 Observations

The VERA observations were carried out on two sets of four adjacent days, on 2011 February 15, 16, 17, 18, and October 20, 21, 23, 24 (details shown in table 1). Two sources within 2°.2 were observed simultaneously by the VERA's dual-beam system (Honma et al. 2003). In the total bandwidth of 256 MHz (16×16 MHz), one of the 16 16-MHz intermediate frequency (IF) channels was assigned to the bright calibrator, 3C 345 in A-beam. The other 15 IF channels were allocated to the target Mrk 501, and NRAO 512 in B-beam (see also figure 1). Left-hand circular polarization (LHCP) signals were received in the Q band, 43115–43131 MHz in A-beam and 42987–43227 MHz in B-beam. The signals were digitized with 2-bit quantization by using the VERA digital filter (Iguchi et al. 2005), and recorded with a rate of 1024 Mbps.

The total observation time is 8 hr per epoch, in which the total on source time is ∼8 hr for 3C 345 in A-beam,

and ∼6 hr for Mrk 501 and ∼2 hr for NRAO 512 in B-beam. The real-time instrumental phase difference data between the two beams were measured with artificial noise sources (Kawaguchi et al. 2000; Honma et al. 2008a). Data correlation was performed with the Mitaka FX correlator (Chikada et al. 1991).

4 Data reduction

Initial calibration on correlated visibilities was performed with the Astronomical Image Processing System (AIPS) software package developed by the National Radio Astronomy Observatory (NRAO). At first, the visibilities were normalized by the auto-correlation with the AIPS task ACCOR and BPASS. *A priori* amplitude calibration was performed with the AIPS task APCAL on the basis of the system equivalent flux density (SEFD) derived from the opacity-corrected system temperature and the antenna gain information for each antenna. The opacity-corrected system temperature was measured with a chopper-wheel method. We adopted the antenna gain with a correction of its dependency on the separation angle between two beams, based on the VERA status report of 2009.[2] The accuracy of the amplitude calibration is ∼10% (e.g., Petrov et al. 2012; Nagai et al. 2013). Secondly, we applied the recalculated delay-tracking solutions to the correlated data (Honma et al. 2007). We adopted the delay-tracking center as $(\alpha_{J2000}, \delta_{2000}) = (16^h53^m52{\overset{s}{.}}216685, +39°45'36{\overset{''}{.}}60894)$ for Mrk 501, $(\alpha_{J2000}, \delta_{2000}) = (16^h42^m58{\overset{s}{.}}809965, +39°48'36{\overset{''}{.}}99399)$ for 3C 345, and $(\alpha_{J2000}, \delta_{2000}) = (16^h40^m39{\overset{s}{.}}632772, +39°46'46{\overset{''}{.}}02849)$ for NRAO 512, taken from the International Celestial Reference Frame 2 (ICRF2: Fey et al. 2010). We also applied an instrumental delay correction table to the data sets on B-beam in order to calibrate dual-beam delay difference (Honma et al. 2008a). After that, we performed fringe fitting on the calibrator 3C 345

---

[2] ⟨http://veraserver.mtk.nao.ac.jp/restricted/CFP2009/status09.pdf⟩.

in the AIPS task FRING to solve delays, rates, and phases by assuming a point source model. The residual phase and gain of 3C 345 were solved by the self-calibration imaging (described in the next paragraph). With the AIPS task CALIB, the phase and gain solutions of self-calibration were obtained using the source structure model. Thirdly, we transferred the derived phase solutions of 3C 345 to NRAO 512 and Mrk 501. After applying the amplitude solutions of Mrk 501 and NRAO 512 obtained by the self-calibration imaging, we obtain the phase-referenced images of these two sources with the CLEAN procedure in the Difmap software package (Shepherd 1997).

We constructed self-calibrated images of all sources. To perform amplitude self-calibration after phase self-calibration converged, we need all the four stations. However, since part of our observations was lacking in one or two stations due to bad weather conditions (see table 1), we combined the visibilities over four adjacent observations by AIPS task DBCON to increase the *uv*-coverage for obtaining precise images. Imaging was performed in Difmap. After careful flagging of bad visibilities and averaging over ∼5 s in the time domain, we constructed the initial structure models by model fitting and self-calibration iteratively. The self-calibrated image parameters are summarized in table 2.

The peak position offsets from the phase-tracking center on the phase-referenced images of Mrk 501 and NRAO 512 were measured with the AIPS task JMFIT. The peak positions measured by model-fitting to the phase-referenced visibilities are consistent with those by JMFIT (typically within ∼10 μas, less than 30 μas) and did not change the results significantly. We derived their radio core positions by subtracting from the JMFIT peak positions of the phase-referenced images the peak position differences between JMFIT to the self-calibrated images and model-fitting to the self-calibrated visibilities (∼1 μas). Then we subtracted the core position of NRAO 512 with reference to 3C 345

from that of Mrk 501 with reference to 3C 345. Thus, we finally obtained the core position of Mrk 501 relative to NRAO 512.

5 Results

5.1 Phase-referenced image qualities

Figure 2 shows the phase-referenced images of Mrk 501 relative to 3C 345's core. The phase-referenced images appear as a point-like source due to the low signal-to-noise ratio (SNR) of the data. We also find NRAO 512 relative to 3C 345's core in the phase-referenced images as a single-component source. The image qualities of all the phase-referenced images are summarized in columns (1)–(5) of table 3. We detect both Mrk 501 and NRAO 512 with an image SNR of higher than nine for all epochs except for the third one, in which two stations suffered from bad weather conditions for over more than half of the observation time. By comparing the peak fluxes of the phase-referenced images in column (3) of table 3 to those of the self-calibrated images in column (2) of table 2, the averaged flux loss ratio is evaluated as typically ∼20%, up to 60% under bad weather conditions.

In the Appendix, the procedure to estimate the position errors is described, and the error values are summarized there in table 5. The position errors are dominated by the tropospheric zenith delay error, by assuming typically ∼2 cm error for VERA (Honma et al. 2008b). Since the theoretically estimated thermal noise error (a few μas, where the image sensitivity is estimated as 1 mJy beam^{-1} by assuming the system noise temperature ∼300 K) does not contribute to the random error (∼20 μas) so much, some other random errors and calibration errors still affect the quality of the phase-referenced images (e.g., Doi et al. 2006). Here we address them as thoroughly as we can. First, there would be a random fluctuation of tropospheric error and geometrical error. Assuming the typical fluctuation of the propagation delay as ∼1 cm d^{-1} (Treuhaft & Lanyi 1987), the position error would be ∼60 μas for the Mrk 501–3C 345 pair, and ∼14 μas for the NRAO 512–3C 345 pair. Secondly, the errors of self-calibration for 3C 345 are also related to the phase-referenced image quality; an antenna-based phase solution with an SNR of ∼8 corresponds to an accuracy of 7° (∼12 μas) theoretically. Thirdly, there would be some errors when we identify the core positions of Mrk 501 and NRAO 512 in the phase-referenced images with Gaussian fitting, because they are not point sources. We evaluate the core identification error in the phase-referenced images as ∼5 μas, by summing the core identification errors (about a few μas in appendix A.1.3) and the Gaussian fit errors (about a few μas) in the self-calibrated images. However, for most

Table 2. Self-calibrated image parameters for 3C 345, Mrk 501, and NRAO 512.*

Source	Epoch	$I_{\rm p}$ (mJy beam^{-1})	$\sigma_{\rm rms}$ (mJy beam^{-1})	$I_{\rm p}/\sigma_{\rm rms}$
	(1)	(2)	(3)	(4)
3C 345	2011/02	2210	30.0	74
	2011/10	2040	17.0	120
Mrk 501	2011/02	280	3.04	92
	2011/10	239	1.78	134
NRAO 512	2011/02	467	5.15	92
	2011/10	541	1.94	278

*(1) Observing epoch, (2) peak intensity, (3) rms of image noise, (4) image dynamic range.

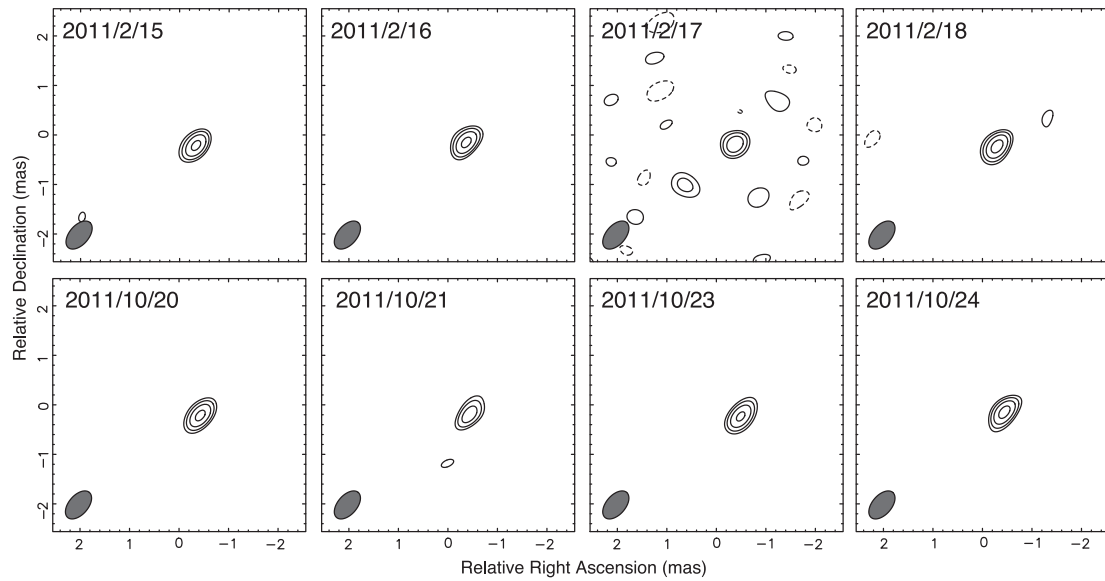**Fig. 2.** Phase-referenced images of Mrk 501's core relative to 3C 345's core. The restored beam size is 0.669 mas × 0.391 mas at a position angle at −40°.9 and the contour starts from three times 28.0 mJy beam^{-1}. The contours are plotted at 3σ noise level × (−1, 1.41, 2, 2.82, 4). Note that the image SNR of the third epoch is much lower than that of all the others due to the bad weather conditions (see table 3).

Table 3. Image qualities and core positions of phase-referenced images.*

Phase-referenced pair	Epoch	I_p (mJy beam^{-1})	σ_{rms} (mJy beam^{-1})	I_p/σ_{rms}	$\Delta\alpha$ (mas)	$\Delta\delta$ (mas)
(1)	(2)	(3)	(4)	(5)	(6)	(7)
Mrk 501–3C 345	2011/02/15	259	29.1	9	-0.33 ± 0.13	-0.21 ± 0.13
	2011/02/16	262	21.0	12	-0.37 ± 0.12	-0.15 ± 0.13
	2011/02/17	224	44.9	5	-0.38 ± 0.14	-0.18 ± 0.14
	2011/02/18	275	30.8	9	-0.30 ± 0.13	-0.23 ± 0.13
	2011/10/20	262	15.5	17	-0.43 ± 0.12	-0.21 ± 0.12
	2011/10/21	210	24.4	9	-0.44 ± 0.13	-0.19 ± 0.13
	2011/10/23	254	18.5	14	-0.50 ± 0.12	-0.23 ± 0.13
	2011/10/24	270	18.4	15	-0.44 ± 0.12	-0.15 ± 0.12
NRAO 512–3C 345	2011/02/15	388	28.5	14	-0.33 ± 0.03	-0.14 ± 0.04
	2011/02/16	408	32.2	13	-0.31 ± 0.03	-0.15 ± 0.04
	2011/02/17	272	61.6	4	-0.28 ± 0.08	-0.12 ± 0.07
	2011/02/18	438	27.5	16	-0.30 ± 0.03	-0.14 ± 0.04
	2011/10/20	228	17.4	13	-0.36 ± 0.04	-0.18 ± 0.04
	2011/10/21	222	25.2	9	-0.32 ± 0.04	-0.23 ± 0.04
	2011/10/23	424	38.4	11	-0.38 ± 0.04	-0.24 ± 0.04
	2011/10/24	410	32.5	13	-0.37 ± 0.04	-0.18 ± 0.04

*(1) The first source is the target source and the second source is the reference source; (2) observing epoch; (3) peak intensity of the target source; (4) image rms noise of the target source; (5) SNR of the target source; (6) and (7) position offset from phase-tracking center of the target source.

epochs, the image SNR of NRAO 512 is comparable to that of Mrk 501, although the angular separation between NRAO 512 and 3C 345 is one-fourth of that of Mrk 501 and 3C 345. This means that the image SNR would not be mainly limited by the error terms depending on the angular separations. We would conservatively overestimate the systematic error (especially for the tropospheric zenith delay error).

5.2 Mrk 501's core position relative to NRAO 512

Figure 3 shows the measured core positions of Mrk 501 relative to NRAO 512 for all the observations as red points and blue points, and they are listed in table 4. The core position error of Mrk 501 relative to NRAO 512 for each epoch given in table 4 is estimated by adding the root sum square of the random error (σ_{random}) to all the other
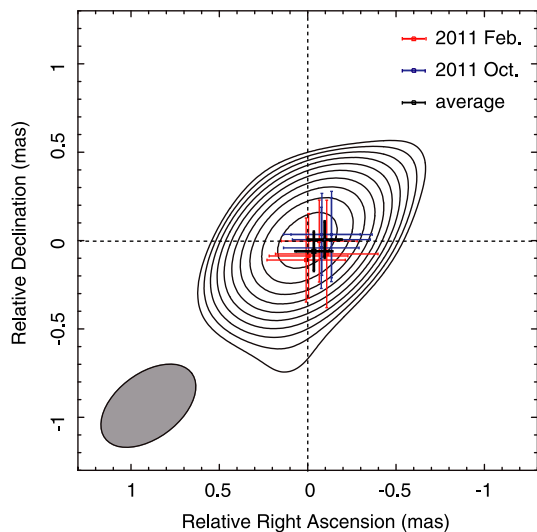
Fig. 3. Self-calibrated image of Mrk 501 in figure 2a is shown with the core positions of Mrk 501 relative to NRAO 512 for all epochs overlaid. The red points represent the core positions over four adjacent days in 2011 February with an averaged positional accuracy of 0.21 mas in RA and 0.22 mas in Dec. The blue points show the core positions over four adjacent days in 2011 October with a positional accuracy of 0.19 mas in RA and 0.20 mas in Dec. Each core position is summarized in table 4. The black points describe the weighted-mean positions over the four days in 2011 February at the relative (RA, Dec) = (−0.03 ± 0.10, −0.05 ± 0.11) mas, and (RA, Dec) = (−0.09 ± 0.10, 0.01 ± 0.10) mas in 2011 October. The origin of this figure corresponds to the phase-tracking center of Mrk 501 and the brightness peak of the self-calibrated image.

Table 4. Core positions of Mrk 501 relative to NRAO 512.[*]

Epoch	$\Delta\alpha$ (mas)	$\Delta\delta$ (mas)
(1)	(2)	(3)
2011/02/15	-0.01 ± 0.20	-0.10 ± 0.20
2011/02/16	-0.06 ± 0.19	0.00 ± 0.20
2011/02/17	-0.10 ± 0.30	-0.10 ± 0.30
2011/02/18	0.01 ± 0.19	-0.10 ± 0.20
2011/10/20	-0.07 ± 0.19	0.00 ± 0.20
2011/10/21	-0.10 ± 0.20	0.00 ± 0.20
2011/10/23	-0.12 ± 0.19	0.00 ± 0.20
2011/10/24	-0.07 ± 0.19	0.00 ± 0.20

[*](1) Observing epoch; (2) and (3) core position of Mrk 501 relative to NRAO 512 in RA and Dec, respectively. These values are derived by subtracting the core position of Mrk 501 relative to 3C 345 from that of NRAO 512 relative to 3C 345, summarized in columns (6) and (7) of table 3 for each epoch. Each position error is estimated as root-sum-square of corresponding error in table 3 (see subsection 5.2).

systematic position errors of Mrk 501 and NRAO 512 relative to the 3C 345 core in table 5, except for the core identification error of 3C 345 (see subsection 5.3 and the Appendix). Typically, the core position error of Mrk 501 relative to NRAO 512 for each epoch is ∼0.20 mas in right ascension (RA) and ∼0.21 mas in declination (Dec), which is around one-third of the major axis of the beam size.

The core positions of Mrk 501 relative to NRAO 512 are distributed in a cluster during four adjacent days in 2011 February and October in the self-calibrated image. During the four adjacent days, the random error, the tropospheric error, and the ionospheric error (σ_{random}, σ_{trop}, and σ_{ion} in table 5) vary randomly. All the other errors, which are the earth orientation parameter error, the antenna position error, the a priori source coordinate error, and the core identification error (σ_{earth}, σ_{ant}, σ_{coord}, and σ_{id} in table 5) are systematic errors. The maximum differences of the core positions within four days are 0.11 ± 0.18 mas and 0.08 ± 0.18 mas in 2011 February and October, respectively. For the errors of the maximum position differences, the common systematic errors are canceled out. We perform a chi-squared test of the phase-referenced core positions over the four adjacent days, and confirm that the core positions of Mrk 501 relative to NRAO 512 coincide

in both RA and Dec with the significance probability of >98%. The weighted mean positions of Mrk 501's core relative to its phase-tracking center over the four adjacent days are $(x, y) = (-0.03 \pm 0.10, -0.05 \pm 0.11)$ mas in 2011 February, and $(x, y) = (-0.09 \pm 0.10, 0.01 \pm 0.10)$ mas in 2011 October, shown as black points in figure 3. Both random and systematic errors of each epoch are used as the weight for calculating the weighted mean positions and their conservative errors. The spatial distribution ranges of the core positions over the four adjacent days are estimated to be $\Theta \sim 0.22$ mas and $\Theta \sim 0.20$ mas in 2011 February and October, respectively, with the statistical significance of $\pm 1\sigma$ (68% confidence level) for the weighted mean position errors. The core positions of Mrk 501 relative to NRAO 512 between 2011 February and October (red crosses and blue crosses in figure 3) could be systematically different, but the difference between the centers of the weighted-mean positions is ∼0.06 mas in both RA and Dec directions, which is less than the spatial distribution ranges of the four adjacent days (∼0.20 mas). Therefore, we find there is no positional change of the radio core in Mrk 501 relative to NRAO 512 within ∼0.20 mas. The discussion is shown in subsection 6.1.

5.3 Core positions of Mrk 501 and NRAO 512 relative to 3C 345's core

Figures 4a and 4b show the core positions of Mrk 501 and NRAO 512 relative to 3C 345's core, respectively. The phase-referenced image qualities, the core positions, and their position errors are summarized in table 3. In the previous subsection, we obtain the core position of Mrk 501
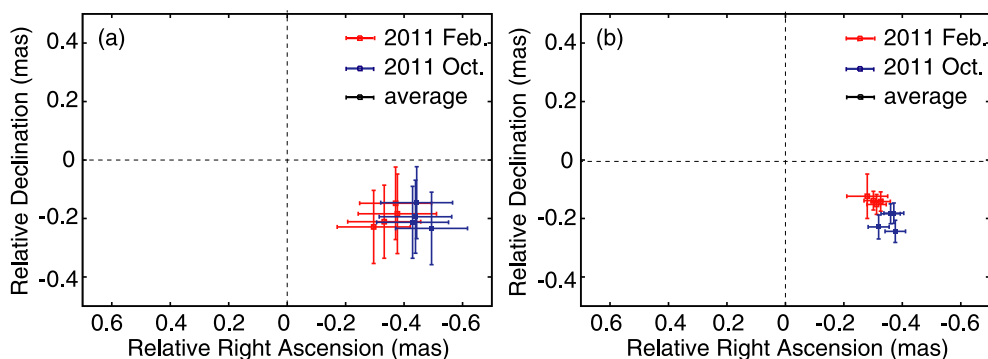
Fig. 4. (a) The core positions of Mrk 501 relative to 3C 345's core, and (b) those of NRAO 512 relative to 3C 345's core. Red points represent four adjacent observations made in 2011 February, blue points represent those in 2011 October, and black points represent the weighted-mean positions over the four adjacent days (see subsection 5.3).

relative to NRAO 512 for each epoch by subtracting the core position in figure 4b from that in figure 4a. Contrary to the derived position offsets from the phase tracking center of Mrk 501's core relative to NRAO 512 (within ~0.09 mas), the position offsets from the phase tracking center of Mrk 501's core relative to 3C 345's core and NRAO 512 relative to 3C 345's core are ~0.4 mas in RA and ~0.2 mas in Dec, which are mainly caused by the position shifts of 3C 345's core.

5.3.1 The Mrk 501 core position relative to 3C 345's core

The position errors of Mrk 501's core relative to 3C 345's core are ~0.12 mas in RA and ~0.13 mas in Dec, summarized in columns (15) and (16) of table 5. From figure 4a, the core positions of Mrk 501 relative to 3C 345 distributes in a cluster over the four adjacent days. The weighted mean positions are $(x, y) = (-0.34 \pm 0.06, -0.19 \pm 0.06)$ mas in 2011 February, and $(x, y) = (-0.45 \pm 0.06, -0.20 \pm 0.06)$ mas in 2011 October. The weighted mean position in 2011 February is ~0.11 mas east of that in 2011 October, which is less than the distribution range (~0.13 mas with $\pm 1\sigma$ error). Thus, there is no positional change of Mrk 501's core relative to 3C 345's core within ~0.13 mas. Note that the phase-referenced positions may include the possible positional change of Mrk 501 ($\lesssim 0.20$ mas) and 3C 345, because neither of them are point sources. Therefore, we do not discuss this result in further detail.

5.3.2 NRAO 512 position relative to 3C 345's core

The position errors of NRAO 512 relative to 3C 345's core are ~0.04 mas both in RA and Dec (table 5). The estimated position errors are about one-fourth of those for Mrk 501's core relative to 3C 345's core mainly due to the tropospheric error based on one-fourth smaller angular separation. In figure 4b, we find the core positions of NRAO 512 relative to 3C 345 in 2011 February (red points) and 2011 October

(blue points) are clearly different. The weighted mean positions are $(x, y) = (-0.31 \pm 0.02, -0.14 \pm 0.02)$ mas in 2011 February, and $(x, y) = (-0.36 \pm 0.02, -0.21 \pm 0.02)$ mas in 2011 October. The weighted mean position in 2011 October is 0.05 ± 0.03 mas west and 0.07 ± 0.03 mas south of that in 2011 February. This result indicates peak position change of 3C 345 by assuming the peak position of NRAO 512 is stationary. The discussion of this is given in subsection 6.2.

6 Discussions

6.1 Application to internal shock model

Here we attempt to constrain bulk Lorentz factors of the jet based the result shown above. We assume that the locations of the unresolved radio-emitting regions in Mrk 501's core at 43 GHz are identical to those of the soft X-ray emitting regions since the radio core is optically thin against SSA. Therefore, the internal shock model can be applicable to our target source Mrk 501.[3] The internal shock model can well explain the various observational properties of soft X- and gamma-ray light-curves in blazars and thus is regarded as one of the leading and standard models for blazar emissions (e.g., Spada et al. 2001; Tanihata et al. 2003; Guetta et al. 2004; Kino et al. 2004; Mimica et al. 2004; Böttcher & Dermer 2010; Joshi & Böttcher 2011). Internal shocks will occur when faster discrete ejecta catch up with slower ones. Electrons are accelerated by the shocks and the non-thermal electromagnetic waves are emitted by these relativistic electrons (e.g., Mimica & Aloy 2010, 2012). Then, denoting the faster ejecta's Lorentz factor as Γ_f, the slower ejecta's

---

[3] Here we do not apply our result to the standing shock model. Recently the original model of the conical standing shock proposed by Marscher et al. (2008) has been improved considering the multi-zone in the standing shock region, "turbulent extreme multi-zone" (TEMZ) model, by Marscher (2014), which also can explain the variability of the soft X-ray light curve of the blazar. For now, our result does not rule out the model because the position of the standing shock is stationary.

Lorentz factor as Γ_s, and the initial separation of the ejecta as I_{IS}, the de-projected distance between the internal-shock position and the central engine (D_{IS}) is given by:

$$D_{IS} \approx 2 \frac{\Gamma_f^2 \Gamma_s^2}{\Gamma_f^2 - \Gamma_s^2} I_{IS} = 2 \frac{(\Gamma_f/\Gamma_s)^2}{(\Gamma_f/\Gamma_s)^2 - 1} \Gamma_s^2 I_{IS}, \quad (1)$$

where $\Gamma_f > \Gamma_s > 1$. In general, such collisions happen repeatedly and multiple internal-shocked regions are generated in the jet flow. The de-projected distributed scale of the shocked regions is, by definition, given by

$$\Delta D_{IS} \equiv D_{IS,max} - D_{IS,min}, \quad (2)$$

where $D_{IS,max}$ is the largest distance between the location of the internal-shocked region and that of the central engine, and $D_{IS,min}$ is the closest one.

The term ΔD_{IS} for Mrk 501 is directly constrained by our VERA astrometric observations. In subsection 5.2, we revealed that the weighted mean core positions of Mrk 501 over the four adjacent days in 2011 February and October were spatially distributed within $\Theta \sim 0.22$ mas and $\Theta \sim 0.20$ mas, respectively, by assuming the radio core of NRAO 512 is stationary. The de-projected distributed scale ΔD_{IS} can be expressed as follows by using the lower limit of the jet viewing angle of $\theta_j \geq 4°$ (Giroletti et al. 2004):

$$\Delta D_{IS} \leq 2.2 \times 10^4 R_s \left(\frac{\Theta}{0.20 \, \text{mas}} \right) \left(\frac{\theta_j}{4°} \right)^{-1}, \quad (3)$$

or $\Delta D_{IS} \leq 1.9$ pc, where 1 mas corresponds to 7.7×10^3 Schwarzschild radii (R_s), or 1 $R_s = 8.6 \times 10^{-5}$ pc. Here we set the lower limit of the central black hole mass of Mrk 501 as $M_{BH} = 0.9 \times 10^9 M_\odot$ in the case of the single black hole (Barth et al. 2002).

The right-hand-side of equation (2) has been constrained by the previous works mentioned below. We set the separation between the ejecta to satisfy $I_{IS} \geq 1 R_s$, because 1 R_s is the minimum dimension of the central engine (e.g., Spada et al. 2001). Tanihata et al. (2003) suggested that the Lorenz factor ratio between the faster and the slower ejecta is $\Gamma_f/\Gamma_s \leq 1.01$ to reproduce the observed X-ray light curves in the flare state. In the quiescent state, Γ_f/Γ_s would be less than that in the flare state because larger Γ_f/Γ_s produces stronger internal shocks closer to the central engine and generates larger energy than smaller Γ_f/Γ_s does, when we assume constant dynamical efficiency and constant I_{IS}. Therefore, we can assume that $(\Gamma_f/\Gamma_s)_{D_{IS}=D_{IS,max}}, (\Gamma_f/\Gamma_s)_{D_{IS}=D_{IS,min}} \leq 1.01$ because during our observation of Mrk 501 was during a relatively quiescent state (just before the X- and γ-ray flare; Bartoli et al. 2012). When we assume Γ_f/Γ_s is constant, $D_{IS,max}$ and $D_{IS,min}$ only depend on the maximum value

of Γ_s ($\Gamma_{s,max}$) and minimum value of Γ_s ($\Gamma_{s,min}$), respectively. Now, ΔD_{IS} can be expressed as a function of only Γ_s. Regarding the minimum value of Γ_s, we adopt $\Gamma_{s,min} \geq 8$ in Mrk 501 (e.g., Kino et al. 2002) based on the minimum among the references of the one-zone SED model fitting. Using equations (2) and (3), we finally constrain a maximum of $\Gamma_{s,max}/\Gamma_{s,min}$ by applying the maximum or minimum values of the above assumptions as follows:

$$\frac{\Gamma_{s,max}}{\Gamma_{s,min}} \leq 2.1 \left[\frac{1}{2} \left(\frac{\Delta D_{IS}}{2.2 \times 10^4 R_s} \right) \right.$$
$$\left. \times \left(\frac{A}{51} \right)^{-1} \left(\frac{I_{IS}}{1 R_s} \right)^{-1} \left(\frac{\Gamma_{s,min}}{8} \right)^{-2} + 1 \right]^{1/2}, \quad (4)$$

where $A \equiv (\Gamma_f/\Gamma_s)^2/[(\Gamma_f/\Gamma_s)^2 - 1]$ and $A \geq 51$. Thus, we find that the maximum-to-minimum ratios of Γ_s during our four adjacent observations are less than 2.1, i.e., $8 \leq \Gamma_s \leq 17$, including the uncertainties of the relevant quantities. The derived Γ_s is roughly comparable to the one estimated by broadband spectra during its quiescent state (e.g., Abdo et al. 2011). Further observations during its flare state are encouraged, to obtain larger ΔD_{IS}.

Using the above Γ_s, we estimate D_{IS}, which corresponds to the distance between the location of the central engine and that of the internal shock, where it corresponds to the location of the radio core. The estimated D_{IS} values are $D_{IS,min} \sim 0.6 \text{pc}(\frac{I_{IS}}{1 R_s})$, and $D_{IS,max} \sim 2.5 \text{pc}(\frac{I_{IS}}{1 R_s})$, and they are comparable to the distance suggested in other blazars (Marscher et al. 2008; Jorstad et al. 2010; Agudo et al. 2011a, 2011b).

6.2 Indication of peak position shift between NRAO 512 and 3C 345

Despite the non-detection of the core position change of the target source Mrk 501, we find a shift of the relative peak positions between the two calibrators, NRAO 512 and 3C 345 (sub-subsection 5.3.2). The relative peak positions of the two quasars form clusters over four adjacent days in 2011 February and October, respectively, and the positions of the clusters are different (see red and blue points in figure 4b). From sub-subsection 5.3.2, the weighted mean position of NRAO 512 relative to 3C 345's core in 2011 October is 0.05 ± 0.03 mas west and 0.07 ± 0.03 mas south of that in 2011 February. This may indicate a shift of 3C 345's core of 0.05 ± 0.03 mas east and 0.07 ± 0.03 mas north from 2011 February to October, when we assume NRAO 512 is a stationary point source. The proper motion of 3C 345's core is estimated to be 0.12 ± 0.04 mas yr^{-1}, equivalent to apparent velocity $4.2 \pm 1.4c$ at a position angle of 36^{+24}_{-27} deg (measured from north to east). Bartel et al. (1986)

performed astrometry between this phase-referencing pair mainly at 8 GHz, and find the proper motions of the core are not significantly different from zero by performing weighted least-squares fits to nine epoch data spanning ∼11 yr. However, focusing on their first three epoch data within one year, the positional change of 3C 345's core was observed towards a similar direction. As for the 3C 345 jet ∼0.60 mas away from the core, we find the proper motion of the absolute position ∼0.40 mas yr^{-1} (apparent velocity ∼14c), which is almost consistent with the result in Bartel et al. (1986), towards a position angle of about −98° (or 72°). Although there is a small difference in the position angle of the proper motion between the jet and the core, a shift of 3C 345's core could be related to the formation of the new jet component, because the large variation of the jet ejection angle has been observed with an amplitude of ∼20° (e.g., Klare et al. 2005; Schinzel et al. 2010). This encourages further astrometric observations.

7 Conclusion

In order to investigate the stationarity of the radio-core position in blazars, we have conducted multi-epoch astrometric VERA observations of the TeV blazar Mrk 501 at 43 GHz for the first time. Below, we summarize the main conclusions in the present work.

(i) In our observation, we achieve an accuracy of ∼0.20 mas for the radio core position of Mrk 501 relative to that of NRAO 512 for each epoch. The relative radio-core positions of Mrk 501 over four adjacent days in 2011 February are distributed within ∼0.22 mas spatial scale, and those in 2011 October are within ∼0.20 mas, respectively, with ±1σ error (68% confidence level) of the weighted-mean position. Comparing the weighted-mean position of the four adjacent observations in 2011 February to that obtained in 2011 October, the difference between these two positions is ∼0.07 mas. Summing up, we find that the radio-core position of Mrk 501 during our observations does not show significant positional change within about 0.20 mas, by assuming the radio-core position of NRAO 512 is stationary.

(ii) By assuming the standard internal shock model, we further constrain the bulk Lorentz factors of the ejecta based on the observational results, i.e., the core position stationarity within 0.20 mas (1.9 pc de-projected). Then we find that the maximum-to-minimum ratio of the slower ejecta's Lorenz factor can be constrained to be $\Gamma_{s,max}/\Gamma_{s,min} \leq 2.1$. The distance between the location of the radio core and that of the central black hole is estimated as a few pc, which is similar to the one indicated in other blazars.

(iii) An indication of core position change between 2011 February and October was found for the phase-referencing pair of 3C 345–NRAO 512. This detection is quite encouraging for the future subsequent observations of blazar core astrometry initiated in the present work.

Further continued astrometric observations targeting large X-ray flares of the TeV blazar Mrk 501 are necessary to explore the locations and stationarity of the radio core. Any simultaneous gamma or radio light curves are also interesting, as are potential changes of the optical polarization position angles (e.g., Marscher et al. 2008).

Acknowledgments

Appendix 1. Error estimation

In this section, we estimate the position errors of the phase-referenced images referencing the error estimations adopted by previous VLBI astrometric studies (e.g., Hada et al. 2011; Reid et al. 1999; Ros et al. 1999). The error terms are the random errors and the uncertainties of ionospheric residuals, tropospheric residuals, core identification process, phase-connection process, instrumental origin, and geometrical parameters (earth orientation parameters, antenna positions and a priori source coordinates; Thompson et al. 2001). In the following subsections, details of major errors are described. Thanks to VERA's dual-beam simultaneous phase-referencing system, the phase-connection errors can be ignored. The instrumental errors are canceled out by applying the dual-beam delay difference table measured with noise sources with ∼0.1 mm accuracy (Honma et al. 2008a). In table 5, we summarize the estimated error budget for each phase-referencing pair in our observations. We consider these errors contribute independently to each other, such that the total position errors for each epoch can be estimated as the root-sum-square of each error.

Table 5. Estimated positional error budgets in the phase-referencing observation by VERA 43 GHz.*

Phase-reference pair (1)	Epoch (2)	$\sigma_{\rm random}$ (3)	(4)	$\sigma_{\rm trop}$ (5)	$\sigma_{\rm ion}$ (6)	$\sigma_{\rm earth}$ (7)	(8)	$\sigma_{\rm ant}$ (9)	(10)	$\sigma_{\rm coord}$ (11)	(12)	$\sigma_{\rm id}$ (13)	(14)	$\sigma_{\rm rss}$ (15)	(16)
Mrk 501−3C 345	2011/02/15	27	26	122	<1	3	5	1	5	2	3	7	16	125	126
	2011/02/16	16	16	122	<1	3	5	1	5	2	3	7	16	123	125
	2011/02/17	56	61	122	<1	3	5	1	5	2	3	7	16	135	137
	2011/02/18	27	26	122	<1	3	5	1	5	2	3	7	16	125	126
	2011/10/20	13	15	122	<1	3	5	1	5	2	3	9	11	123	124
	2011/10/21	23	28	122	<1	3	5	1	5	2	3	9	11	125	126
	2011/10/23	16	21	122	<1	3	5	1	5	2	3	9	11	123	125
	2011/10/24	16	16	122	<1	3	5	1	5	2	3	9	11	123	124
NRAO 512−3C 345	2011/02/15	18	16	28	<1	3	5	1	5	2	3	7	16	33	38
	2011/02/16	17	17	28	<1	3	5	1	5	2	3	7	16	33	37
	2011/02/17	64	70	28	<1	3	5	1	5	2	3	7	16	76	72
	2011/02/18	15	14	28	<1	3	5	1	5	2	3	7	16	32	36
	2011/10/20	17	18	28	<1	3	5	1	5	2	3	9	11	35	36
	2011/10/21	22	29	28	<1	3	5	1	5	2	3	9	11	42	38
	2011/10/23	21	24	28	<1	3	5	1	5	2	3	9	11	38	38
	2011/10/24	18	20	28	<1	3	5	1	5	2	3	9	11	36	36

*(1) The first source is the target source and the second source is the reference source; (2) observing epoch; (3) and (4) the random errors estimated by the beamwidth over two times SNR in RA and Dec; (5) the tropospheric residual errors; (6) the ionospheric residual errors; (7) and (8) the Earth orientation parameter errors in RA and Dec; (9) and (10) the antenna position errors in RA and Dec; (11) and (12) a priori source coordinates errors in RA and Dec. The error contributions from the geometrical errors (7–12) are estimated based on the simulation presented in Pradel, Charlot, and Shibata (2006). (13) and (14) The core identification error of 3C 345 in RA and Dec, respectively. (15) and (16) Total errors in RA and Dec are estimated as the root-sum-square of each error. The units are in μas.

A.1.1. Random

In columns (3) and (4) of table 5 we summarize the random error of all phase-referenced images in RA and Dec, respectively. The position error can be expressed as $\theta_{\rm b}/(2\,SNR)$ (Thompson et al. 2001), where θ_b is each interferometric beam size in RA or Dec ($\theta_b \sim 0.6$ mas $\times$ 0.4 mas at a position angle of $\sim 130°$), and SNR is the signal-to-noise ratio of the phase-referenced images (see column 5 of table 3). The SNR of the phase-referenced images achieved is ~ 11 on average.

A.1.2. Propagation delay

Here we briefly review how to estimate the contribution of the propagation delay error to the phase-referenced position error. The effects of the propagation delay error at each station cause a decrease in SNR of the phase-referenced images and image shift. The position error $\delta\theta$ originated from the phase error $\Delta\phi$ is expressed as $\delta\theta = \Delta\phi \cdot (2\pi D_\lambda)^{-1}$ (e.g., Thompson et al. 2001), where $D_\lambda \sim D\,\lambda^{-1}$, D is the baseline length, and λ is the observing wavelength. $\Delta\phi$ is estimated by $2\pi c\Delta\tau\lambda^{-1}$, where c is the speed of light and $\Delta\tau$ is the propagation delay error. $\Delta\tau$ can be approximated by $\delta\tau_0 \sec Z$, where $\delta\tau_0$ is the residual vertical delay and Z is the local source zenith angle. When the two phase-referencing pairs separate in zenith angle by ΔZ, the

position error $\delta\theta$ caused by the propagation delay error for a single antenna is estimated as a first-order Taylor expansion of τ as follows (Reid et al. 1999):

$$\delta\theta \sim \frac{c\delta\tau_0}{D} \sec Z \tan Z \Delta Z. \tag{A1}$$

The propagation delays are mainly caused by the ionospheric and tropospheric medium. In columns (5) and (6) of table 5, the tropospheric error and ionospheric error of each phase-referencing pair are summarized. The propagation delays caused by the tropospheric medium are independent of observing frequency, while those caused by the ionospheric medium are inversely proportional to the square of the frequency. Therefore, we omit a detailed description of the ionospheric error, because it is estimated to be $<1\,\mu$as at 43 GHz. Since the tropospheric zenith delays are typically within ~ 2 cm accuracy for VERA (Honma et al. 2008b), the position errors can be estimated as $\delta\theta \sim 122\,\mu$as for $\Delta Z = 2°09$ (Mrk 501–3C 345 pair), and $\sim 28\,\mu$as for $\Delta Z = 0°49$ (NRAO 512–3C 345 pair) at 43 GHz, $Z \sim 50°$ and $D = 2.3 \times 10^3$ m.

A.1.3. Core identification

The core identification error indicates the possible slight difference between the fitted Gaussian peak and the actual brightness peak, and would come from the blending of the

core and the jet structure. To clarify the source structure, we produced the self-calibrated images of all the three sources (see figure 1 and section 4).

We identified the core of 3C 345 by model fitting to the calibrated visibility data, and found it has the bright jet structure. The core was well modeled by an elliptical Gaussian model, and the jet emission was modeled as one or two circular Gaussians. We defined the center of each Gaussian model as the component position. To evaluate the core identification error, we derived the differences between the center of the elliptical Gaussian and the position of the brightness-peak pixels in super-resolution maps measured by the AIPS task MAXFIT. The super-resolution maps were convolved by a circular Gaussian beam of full-width at half-maximum (FWHM) about a half of the minor axes of the synthesized beams. The maximum core identification error was estimated as $16 \, \mu$as, and all the position errors are summarized in columns (13) and (14) of table 5. However, by subtracting the core position of NRAO 512 relative to 3C 345 from the core position of Mrk 501 relative to 3C 345, the core identification error of calibrator 3C 345 is completely cancelled out.

For Mrk 501 and NRAO 512, we estimated the core identification error in the same manner. The position differences between visibility-based model-fitting and MAXFIT were negligible, typically less than a few μas.

References

Abdo, A. A., et al. 2010, Nature, 463, 919
Abdo, A. A., et al. 2011, ApJ, 727, 129
Agudo, I., et al. 2011a, ApJ, 726, L13
Agudo, I., et al. 2011b, ApJ, 735, L10
Bartel, N., Herring, T. A., Ratner, M. I., Shapiro, I. I., & Corey, B. E. 1986, Nature, 319, 733
Barth, A. J., Ho, L. C., & Sargent, W. L. W. 2002, ApJ, 566, L13
Bartoli, B., et al. 2012, ApJ, 758, 2
Böttcher, M., & Dermer, C. D. 2010, ApJ, 711, 445
Chikada, Y., Kawaguchi, N., Inoue, M., Morimoto, M., Kobayashi, H., & Mattori, S. 1991, in Frontiers of VLBI, ed. H. Hirabayashi et al. (Tokyo: Universal Academy Press), 79
Doi, A., et al. 2006, PASJ, 58, 777
Fey, A. L., et al. 2004, AJ, 127, 3587
Fey, A. L., Gordon, D., & Jacobs, C. S. 2010, in IERS/IVS Working Group, The Second Realization of the International Celestial Reference Frame by Very Long Baseline Interferometry, IERS Technical Note No. 35 (Frankfurt: International Earth Rotation and Reference Systems Service)
Giroletti, M., Giovannini, G., Cotton, W. D., Taylor, G. B., Pérez-Torres, M. A., Chiaberge, M., & Edwards, P. G. 2008, A&A, 488, 905
Giroletti, M., Giovannini, G., Taylor, G. B., & Falomo, R. 2004, ApJ, 613, 752
Guetta, D., Ghisellini, G., Lazzati, D., & Celotti, A. 2004, A&A, 421, 877
Hada, K., Doi, A., Kino, M., Nagai, H., Hagiwara, Y., & Kawaguchi, N. 2011, Nature, 477, 185
Honma, M., et al. 2003, PASJ, 55, L57
Honma, M., et al. 2007, PASJ, 59, 889
Honma, M., et al. 2008a, PASJ, 60, 935
Honma, M., Tamura, Y., & Reid, M. J. 2008b, PASJ, 60, 951
Iguchi, S., Kurayama, T., Kawaguchi, N., & Kawakami, K. 2005, PASJ, 57, 259
Jorstad, S. G., et al. 2010, ApJ, 715, 362
Joshi, M., & Böttcher, M. 2011, ApJ, 727, 21
Jung, T., Sohn, B. W., Kobayashi, H., Sasao, T., Hirota, T., Kameya, O., Choi, Y. K., & Chung, H. S. 2011, PASJ, 63, 375
Kawaguchi, N., Sasao, T., & Manabe, S. 2000, in SPIE Conf. Proc. 4015, Radio Telescopes, ed. H. R. Butcher (Bellingham, WA: SPIE), 544
Kellermann, K. I., & Pauliny-Toth, I. I. K. 1981, ARA&A, 19, 373
Kino, M., Mizuta, A., & Yamada, S. 2004, ApJ, 611, 1021
Kino, M., Takahara, F., & Kusunose, M. 2002, ApJ, 564, 97
Klare, J., Zensus, J. A., Lobanov, A. P., Ros, E., Krichbaum, T. P., & Witzel, A. 2005, in ASP Conf. Ser. 340, Future Directions in High Resolution Astronomy, ed. J. Romney & M. Reid (San Francisco: ASP), 40
Komatsu, E., et al. 2009, ApJS, 180, 330
Lanyi, G. E., et al. 2010, AJ, 139, 1695
Ma, C., et al. 1998, AJ, 116, 516
Marscher, A. P. 2014, ApJ, 780, 87
Marscher, A. P., et al. 2008, Nature, 452, 966
Marscher, A. P., & Gear, W. K. 1985, ApJ, 298, 114
Mimica, P., & Aloy, M. A. 2010, MNRAS, 401, 525
Mimica, P., & Aloy, M. A. 2012, MNRAS, 421, 2635
Mimica, P., Aloy, M. A., Müller, E., & Brinkmann, W. 2004, A&A, 418, 947
Nagai, H., et al. 2013, PASJ, 65, 24
Petrov, L., Honma, M., & Shibata, S. M. 2012, AJ, 143, 35
Pradel, N., Charlot, P., & Lestrade, J.-F. 2006, A&A, 452, 1099
Reid, M. J., Readhead, A. C. S., Vermeulen, R. C., & Treuhaft, R. N. 1999, ApJ, 524, 816
Ros, E., Marcaide, J. M., Guirado, J. C., Ratner, M. I., Shapiro, I. I., Krichbaum, T. P., Witzel, A., & Preston, R. A. 1999, A&A, 348, 381
Schinzel, F. K., Lobanov, A. P., & Zensus, J. A. 2010, in ASP Conf. Ser. 427, Accretion and Ejection in AGN: a Global View, ed. L. Maraschi (San Francisco: ASP), 153
Shapiro, I. I., et al. 1979, AJ, 84, 1459
Shepherd, M. C. 1997, in ASP Conf. Ser. 125, Astronomical Data Analysis Software and Systems VI, ed. G. Hunt & H. Payne (San Francisco: ASP), 77
Spada, M., Ghisellini, G., Lazzati, D., & Celotti, A. 2001, MNRAS, 325, 1559
Tanihata, C., Takahashi, T., Kataoka, J., & Madejski, G. M. 2003, ApJ, 584, 153
Thompson, A. R., Moran, J. M., & Swenson, G. W., Jr. 2001, Interferometry and Synthesis in Radio Astronomy, 2nd ed. (New York: Wiley), 467
Titov, O., Lambert, S. B., & Gontier, A.-M. 2011, A&A, 529, A91
Treuhaft, R. N., & Lanyi, G. E. 1987, Radio Science, 22, 251